JGR Biogeosciences

RESEARCH ARTICLE
10.1029/2025JG009003

Impact of Spatial Scale on the Performance of a Photoacclimation Model

Dongmei Lian[1], Zhongping Lee[1], Shaoling Shang[1], Shuaixing Peng[1], and Xin Liu[2]

[1]State Key Laboratory of Marine Environmental Science, College of Ocean and Earth Sciences, Xiamen University, Xiamen, China, [2]State Key Laboratory of Marine Environmental Science, College of the Environment and Ecology, Xiamen University, Xiamen, China

Key Points:

- Matches between photoacclimation model and satellite estimates are poor at small scales but improve significantly as the scale increases
- The high dependency of photoacclimation model on spatial scale persists whether for the same or mixed levels of chlorophyll variation
- Scale-dependent model constants may limit the applicability, emphasizing the need to develop a broadly applicable model

Correspondence to:
Z. Lee,
zhongping.lee@umb.edu

Citation:
Lian, D., Lee, Z., Shang, S., Peng, S., & Liu, X. (2025). Impact of spatial scale on the performance of a photoacclimation model. *Journal of Geophysical Research: Biogeosciences*, *130*, e2025JG009003. https://doi.org/10.1029/2025JG009003

Received 10 APR 2025
Accepted 23 SEP 2025

Author Contributions:
Conceptualization: Zhongping Lee
Formal analysis: Dongmei Lian
Funding acquisition: Zhongping Lee, Shaoling Shang
Investigation: Dongmei Lian
Methodology: Zhongping Lee
Project administration: Zhongping Lee, Shaoling Shang
Supervision: Zhongping Lee, Shaoling Shang
Validation: Shuaixing Peng
Visualization: Dongmei Lian, Shuaixing Peng
Writing – original draft: Dongmei Lian
Writing – review & editing: Dongmei Lian, Zhongping Lee, Shaoling Shang, Xin Liu

Abstract Due to the photoacclimation of phytoplankton chlorophyll pigments, it is critical to know the ratio of carbon-to-chlorophyll (θ) if one wants to estimate phytoplankton carbon from chlorophyll or vice versa. Behrenfeld et al. (2016, https://doi.org/10.1038/nclimate2838) developed a widely used model to estimate θ based on solar radiation within the mixed layer, which reproduced θ very well for the areas defined in the study, but there is a knowledge gap regarding whether this model is applicable to any spatial scale. Here, we evaluated the performance of this model for areas of different sizes and found that the agreement between model-calculated θ and satellite-estimated θ is highly dependent on the size of the interested area where the agreement is very poor (R^2 is as low as ~0.05) if the size is small. As the size of an interested area increases, the agreement between model estimates and satellite retrievals improves significantly (R^2 is as high as ~0.80). This trend or pattern persists regardless of whether the area is constrained within the same level or mixed levels of chlorophyll variation. These results highlight that the applicability of this popular model of carbon-to-chlorophyll ratio should be better applied to oceanic areas matching those used in the model development and underscore the need to develop a more universally applicable model for the photoacclimation of phytoplankton chlorophyll in the upper ocean.

Plain Language Summary Phytoplankton play a crucial role in the ocean; understanding the ratio of carbon to chlorophyll (θ) is essential for estimating phytoplankton carbon from chlorophyll levels or vice versa. A widely used model developed by Behrenfeld et al. (2016, https://doi.org/10.1038/nclimate2838) estimates θ based on solar radiation in the mixed layer and has been effective in specific study areas. However, its applicability to areas of different sizes has not been fully explored. In this study, we assessed the performance of this model across areas of varying spatial sizes. We found that the agreement between satellite-based estimates of θ and the model results are strongly influenced by the spatial size of the area of interest. For smaller areas, there is a low correlation between model results and satellite data. As the spatial size of the area increases, the correlation improves significantly. This pattern holds regardless of whether the areas exhibit similar or varying levels of chlorophyll. These results suggest that the model is most suitable for the specific spatial scales for which it was originally designed. They also highlight the need for a more universally applicable model to estimate the carbon-to-chlorophyll ratio in the future.

1. Introduction

Phytoplankton are the primary producers of the global ocean, which are critical constituents of the ecosystem. In the past, chlorophyll concentration (Chl) has been regarded as the proxy for phytoplankton biomass, as generally there is a very positive relationship between the contents of phytoplankton and Chl. However, recent research has demonstrated that Chl is also regulated by physiological photoacclimation (Letelier et al., 1993; Mignot et al., 2014). In other words, due to different exposure to solar radiation, while Chl may change, phytoplankton biomass remains the same. To quantitatively interpret the impact of solar radiation on Chl in the upper ocean, Behrenfeld et al. (2016) developed a photoacclimation model to quantify the ratio (θ) of phytoplankton carbon (C_{ph}) to Chl, which is exclusively driven by light availability. It is found that the areal averaged ratio of designated areas calculated from the model ($\overline{\theta_{Model}}$) agreed excellently with that obtained from satellite ocean color products ($\overline{\theta_{Sat}}$). It thus suggests that photoacclimation is a dominant process controlling the dynamics of phytoplankton θ in the upper ocean (Bellacicco et al., 2016; He et al., 2021; Xiu & Chai, 2021), although other factors such as ecological mechanisms could also impact this ratio (e.g., Bianchi, 2011; Chang et al., 2003; Hung et al., 2010; Hung & Gong, 2011; Xing et al., 2019). Moreover, findings also suggested that the observed Chl reduction with

future rising temperatures likely reflects physiological adjustments rather than a decline in biomass (da Silveira Bueno et al., 2024; Dutkiewicz et al., 2019; Yamaguchi et al., 2022). This insight offers a more optimistic perspective on the impacts of global warming on marine phytoplankton (Behrenfeld et al., 2016).

The photoacclimation model (θ_{model} hereafter) of C_{ph} to Chl ratio is expressed as a function of sea surface photosynthetically available radiation (PAR0), the diffuse attenuation coefficient for PAR (K_{PAR}), and the mixed-layer depth (MLD) (see details in Data and Methods). In this model, there are two model constants (c_1 and c_2) that significantly influence its performance. To determine these constants, Behrenfeld et al. (2016) divided the global ocean into 37 areas (or "bins") based on the Chl variance level, with Chl of the global ocean referring to the 8-day Chl product from the Moderate Resolution Imaging Spectroradiometer on the Aqua satellite (MODIS Aqua) (Behrenfeld et al., 2005, 2016). Specifically, the area of Level 0 (L0) covers waters with 0 < standard deviation of Chl (s.d.Chl) < 0.018 mg m^{-3}, L1 for 0.018 < s.d.Chl < 0.026 mg m^{-3}, L2 for 0.026 < s.d.Chl < 0.09 mg m^{-3}, L3 for 0.09 < s.d.Chl < 0.4 mg m^{-3}, and L4 for s.d.Chl > 0.4 mg m^{-3} (Behrenfeld et al., 2005, 2016). For pixels in each bin, θ_{Sat} at every pixel ($\theta_{Sat\text{-}pix}$) was calculated from MODIS-produced Chl and C_{ph} (which is converted from particle backscattering coefficient, b_{bp}) and $\overline{\theta_{Sat}}$ was obtained by averaging the $\theta_{Sat\text{-}pix}$ values of all pixels within this bin. For MODIS data in the period of 2002–2014 and for the 8-day global composites, the averages of the 37 bins generated 19,246 total number of observed $\overline{\theta_{Sat}}$, which were then used to fit in the model and resulted in the values of c_1 and c_2 (see details in Behrenfeld et al. (2016)).

Although it is exciting that this photoacclimation model worked very well for the average of these bins and its conclusions were adopted by many studies (Burt et al., 2018; Fox et al., 2020; He et al., 2021; Sharma et al., 2019; Yang et al., 2021), it is not clear if the remotely sensed and model-calculated θ could also match well for areas of any size. This information is crucial for applying this model to a random area particularly when converting Chl to C_{ph} or vice versa for that region. In addition, independent of spatial scale, the satellite-derived Chl—and thus the relationship between θ_{Sat} and θ_{model}—may also be influenced by optical interference from colored dissolved organic matter and terrestrially derived dissolved organic carbon, which are often introduced by typhoons and riverine discharges (Liu et al., 2013; Swan et al., 2009; Tang et al., 2008), although evaluating these effects is beyond the scope of this study.

In this study, we thus investigated the impacts of bin sizes on the relationship between remotely sensed and model-calculated θ with the objective of obtaining an in-depth understanding of the applicability of this widely adopted photoacclimation model for phytoplankton in the oceans. From analyses of various bin sizes, we found that there is a high dependency of model performance on areal size, indicating the need for continued efforts to improve the modeling of phytoplankton photoacclimation in the ocean.

2. Materials and Methods

2.1. The Photoacclimation Model

The model (θ_{model}) of C_{ph} to Chl ratio is described by a series of equations (Behrenfeld et al., 2016), which are described in detail below.

$$\theta_{Model} = \theta_{DM}\,\Delta\theta_{SM} \tag{1}$$

Here, θ_{DM} is a "baseline" deep-mixing solution, representing photoacclimation in a deep-mixing scenario where the MLD is deeper than the euphotic zone depth (Z_{eu}) with $\Delta\theta_{SM}$ a correction factor for shallow mixing.

θ_{DM} is modeled as Equation 2, which has two inputs: PAR0 and K_{PAR}.

$$\theta_{DM} = c_1\, e^{c_2 \frac{PAR0^{0.45}}{K_{PAR}}} \tag{2}$$

c_1 and c_2 are the constants of this model, which are, respectively, 19 g C (g Chl)$^{-1}$ and 0.038 m^{-1} (Einstein m^{-2} hr^{-1})$^{-0.45}$.

For situations of shallow mixed layers (MLD < Z_{eu}), a variable $\Delta\theta_{SM}$ (see Equations 3 and 4) is introduced to make an adjustment,

$$\Delta\theta_{SM} = \begin{cases} \dfrac{1 + e^{-0.15\ PAR0}}{1 + e^{-3\ I_{ML}}}, & MLD < \dfrac{6}{K_{PAR}} \quad (3) \\ 1, & MLD \geq \dfrac{6}{K_{PAR}} \quad (4) \end{cases}$$

Here, I_{ML} is the irradiance at half of the MLD and calculated following Equation 5 (Behrenfeld et al., 2005; Westberry et al., 2008):

$$I_{ML} = PAR0\ e^{-0.5\ K_{PAR}\ MLD} \quad (5)$$

Thus, Equations 1–5 indicate that the ratio of θ is solely a function of solar radiation in the upper water column, which is the essence of phytoplankton photoacclimation.

2.2. Inputs of the Photoacclimation Model and Data Source

Standard Level 3 products of PAR0 (Einstein $m^{-2}\ d^{-1}$) and the diffuse attenuation coefficient at 490 nm ($K_d(490)$) estimated from MODIS Aqua measurements were downloaded from the National Aeronautics and Space Administration (NASA) Ocean Color Webpage (https://oceancolor.gsfc.nasa.gov/). To ensure consistency with the photoacclimation model developed by Behrenfeld et al. (2016), $K_d(490)$ was calculated using the 490–547 band ratio algorithm (Austin & Petzold, 1981; Mueller, 2000; Werdell & Bailey, 2005). K_{PAR} was calculated from $K_d(490)$, which is an empirical conversion between $K_d(490)$ and K_{PAR} (Morel et al. (2007)). These data covered the period from July 2002 to December 2020 with a spatial resolution of 9 km and an 8-day temporal resolution. Following Kirk (1983), day length (in hours) was determined as a function of date and latitude. Day length was then used to convert the daily PAR0 product to hourly PAR0 (Einstein $m^{-2}\ hr^{-1}$). The MLD data were obtained from the HYbrid Coordinate Ocean Model (HYCOM, https://www.hycom.org/) with the same spatial and temporal resolutions as the aforementioned satellite data for the same period.

2.3. Method of Obtaining Areal Averages

To assess the performance of $\overline{\theta_{Model}}$ for different bin sizes, $\overline{\theta_{Sat}}$ of each pixel was calculated following Behrenfeld et al. (2016). Chl, estimated with the Ocean Color Index algorithm (Hu et al., 2012) from the MODIS Aqua measurements, was downloaded from the NASA Ocean Biology Processing Group at the temporal and spatial resolutions mentioned above. Following Behrenfeld et al. (2005) and Westberry et al. (2008), C_{ph} was converted from the particle backscattering coefficient at 443 nm ($b_{bp}(443)$) from the MODIS Aqua measurements and estimated by the Garver-Siegel-Maritorena algorithm ($b_{bp(443)}^{GSM}$) (Maritorena et al., 2002). In all cases of our study, we first computed $\theta_{Sat\text{-}pix}$, then obtained average values ($\overline{\theta_{Sat}}$) for each specific area of interest. Similarly, for $\overline{\theta_{Model}}$ of a bin, we calculated θ_{Model} for each pixel ($\theta_{Model\text{-}pix}$) first, and subsequently determined the average values for each designated area ($\overline{\theta_{Model}}$). Thus, each plot in the figures (i.e., the subsequent Figures 1, 3, 7, and 9) represents the average of all pixels within a study area over an 8-day period, which is consistent with that of Behrenfeld et al. (2016).

2.4. Study Area and Level of Chl Variance

For the development of the photoacclimation model, Behrenfeld et al. (2016) focused on the bins within the same variance level of Chl. Thus, for consistency, we first focused on the change in bin sizes exclusively within the same variance level of Chl. Subsequently, we also changed the bin sizes across different variance levels of Chl. Following Behrenfeld et al. (2016), five variance levels of Chl were defined (as stated earlier, L0 to L4) with each level determined based on the standard deviation of Chl (s.d. Chl). For the purpose of demonstration, we focused on the Pacific Ocean because it exhibited the best agreement between $\overline{\theta_{Sat}}$ and $\overline{\theta_{Model}}$ among the 37 studied areas or bins. Especially, according to Behrenfeld et al. (2016), $\overline{\theta_{Sat}}$ and $\overline{\theta_{Model}}$ had excellent agreements for L0, L1, and L2 of the South Pacific Ocean (SP) and for L2 and L3 of the North Pacific Ocean (NP).

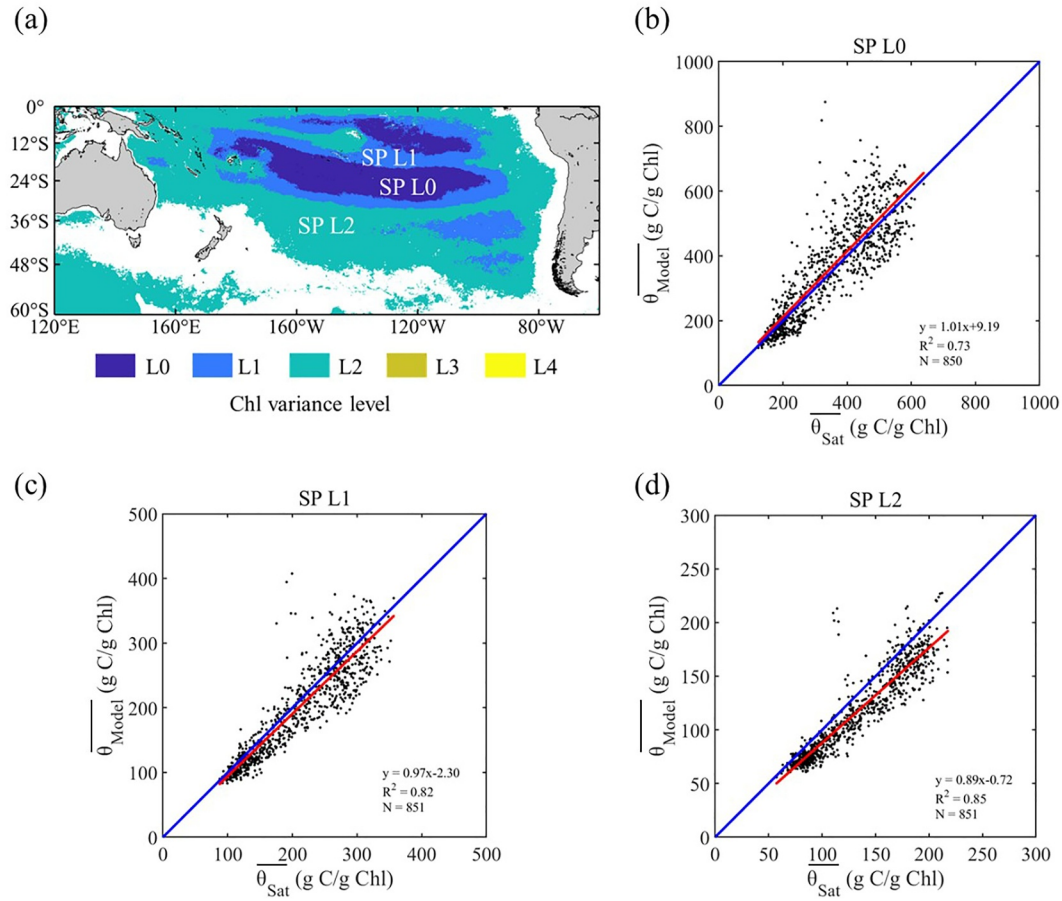

Figure 1. Relationship between $\overline{\theta_{Sat}}$ and $\overline{\theta_{Model}}$ in three bins of South Pacific (SP). (a) The study areas of the three bins with background colors representing different Chl variance levels. (b)–(d) The relationships between $\overline{\theta_{Sat}}$ and $\overline{\theta_{Model}}$ for bins of SP L0, SP L1, and SP L2, respectively. The blue line is a 1:1 line, and the red line is a linear fit. N is the number of plotting data.

2.5. Validation of Data Processing

To ensure data processing of this study is consistent with that of Behrenfeld et al. (2016), we replicated the comparison between $\overline{\theta_{Model}}$ and $\overline{\theta_{Sat}}$ as performed in their study. As examples, we concentrated on the regions designated as SP L0, L1, and L2 (Figure 1a). By replicating this comparison, we aimed to validate results from our data processing matching those of Behrenfeld et al. (2016), as such a consistency check is crucial for assessing the model performance over different sizes of bins.

Following Behrenfeld et al. (2016), $\overline{\theta_{Model}}$ were compared with $\overline{\theta_{Sat}}$ for the three bins in the SP and for the period of 2002–2020. It is found that all of them have a statistically significant relationship ($p < 0.01$ in t-test). For SP L0, $\overline{\theta_{Sat}}$ ranged from ~123.0 to 638.5 g C (g Chl)$^{-1}$, whereas $\overline{\theta_{Model}}$ ranged from ~116.0 to 875.0 g C (g Chl)$^{-1}$ (Figure 1b). The coefficient of determination (R^2) and the slope values between $\overline{\theta_{Sat}}$ and $\overline{\theta_{Model}}$ were 0.73 and 1.01, respectively. The fitting line is almost approaching the 1:1 line. A similar pattern was observed in SP L1 where $\overline{\theta_{Sat}}$ ranged from ~87.6 to 356.6 g C (g Chl)$^{-1}$, whereas $\overline{\theta_{Model}}$ ranged from ~83.2 to 407.4 g C (g Chl)$^{-1}$ (Figure 1c). The R^2 and slope values between $\overline{\theta_{Sat}}$ and $\overline{\theta_{Model}}$ were 0.82 and 0.97, respectively, also with the fitting line nearing the 1:1 line. Although in SP L2, the range of $\overline{\theta_{Sat}}$ ranged from ~57.5 to 217.6 g C (g Chl)$^{-1}$, and the range of $\overline{\theta_{Model}}$ from ~55.8 to 227.4 g C (g Chl)$^{-1}$ (Figure 1d). The R^2 and slope values between $\overline{\theta_{Sat}}$ and $\overline{\theta_{Model}}$ were 0.85 and 0.89, respectively. It seems that $\overline{\theta_{Model}}$ is slightly lower than $\overline{\theta_{Sat}}$ in SP L2, whereas the same pattern is also displayed by Behrenfeld et al. (2016) (their Figure 4b and Figure S8). The fitting line in SP L2 still closely approaches the 1:1 line, although slightly below it. All these results are consistent with those showing in

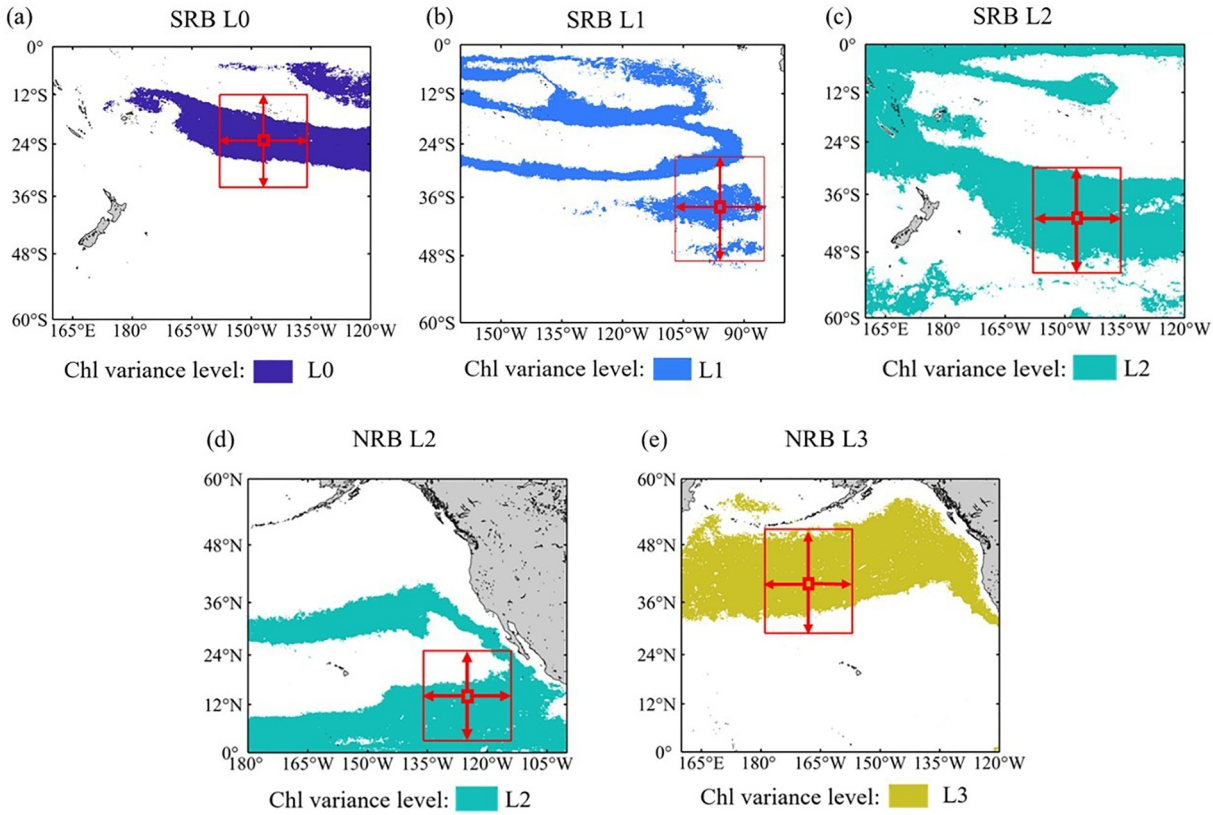

Figure 2. The study areas of bin-size expansion in single Chl variation level. These random study areas are South Random Bin (SRB) L0 (a), SRB L1 (b), SRB L2 (c), North Random Bin (NRB) L2 (d), and NRB L3 (e), respectively. The background color of Chl variance levels in Pacific Ocean. Navy blue: L0, light blue: L1, green: L2, dark yellow: L3. The small red box represents the initial bin size (2° × 2°), and the large box represents the expanded final bin size (22° × 22°), following the directions of arrows.

Behrenfeld et al. (2016) (their Figure 4b and Figure S8), indicating that the data processing in our study is valid and suitable for this effort.

2.6. Statistical Analyses

Following Behrenfeld et al. (2016), for each pixel within the bins defined above, $\theta_{\text{Sat-pix}}$ and $\theta_{\text{Model-pix}}$, respectively, were calculated; subsequently, the $\overline{\theta_{\text{Sat}}}$ and $\overline{\theta_{\text{Model}}}$ were obtained for each bin. Thus, we obtained the pairs of $\overline{\theta_{\text{Sat}}}$ and $\overline{\theta_{\text{Model}}}$ for each bin size for the 8-day time series from July 2002 to December 2020. A one-sample *t*-test was employed to determine differences between two data sets (i.e., $\overline{\theta_{\text{Sat}}}$ and $\overline{\theta_{\text{Model}}}$), and the *p*-value ($p$) was used to assess statistical significance (Gerald, 2018). To assess the correspondence between $\overline{\theta_{\text{Sat}}}$ and $\overline{\theta_{\text{Model}}}$, R^2 and the slope from linear regression analyses were calculated. The linear regression analyses were computed using the "cftool" function of MATLAB Version 2019a (The MathWorks, Inc., Natick, Massachusetts, United States). If $\overline{\theta_{\text{Sat}}}$ closely match $\overline{\theta_{\text{Model}}}$, it suggests that θ dynamics are primarily driven by photoacclimation and the robustness of the photoacclimation model (Behrenfeld et al., 2016). Conversely, significant deviations between the two will indicate a limitation of the model (Behrenfeld et al., 2016).

3. Results

3.1. Model Performance of Varying Bins Within the Same Variance Level of Chl

First, to gauge the relationship between model performance and bin size for pixels within the same variance level of Chl, we randomly selected a 2° × 2° bin in the Pacific Ocean and then expanded the bin to 22° × 22° with a step of 2° × 2° (Figure 2); subsequently, we compared $\overline{\theta_{\text{Sat}}}$ with $\overline{\theta_{\text{Model}}}$ for each bin. These randomly selected areas or

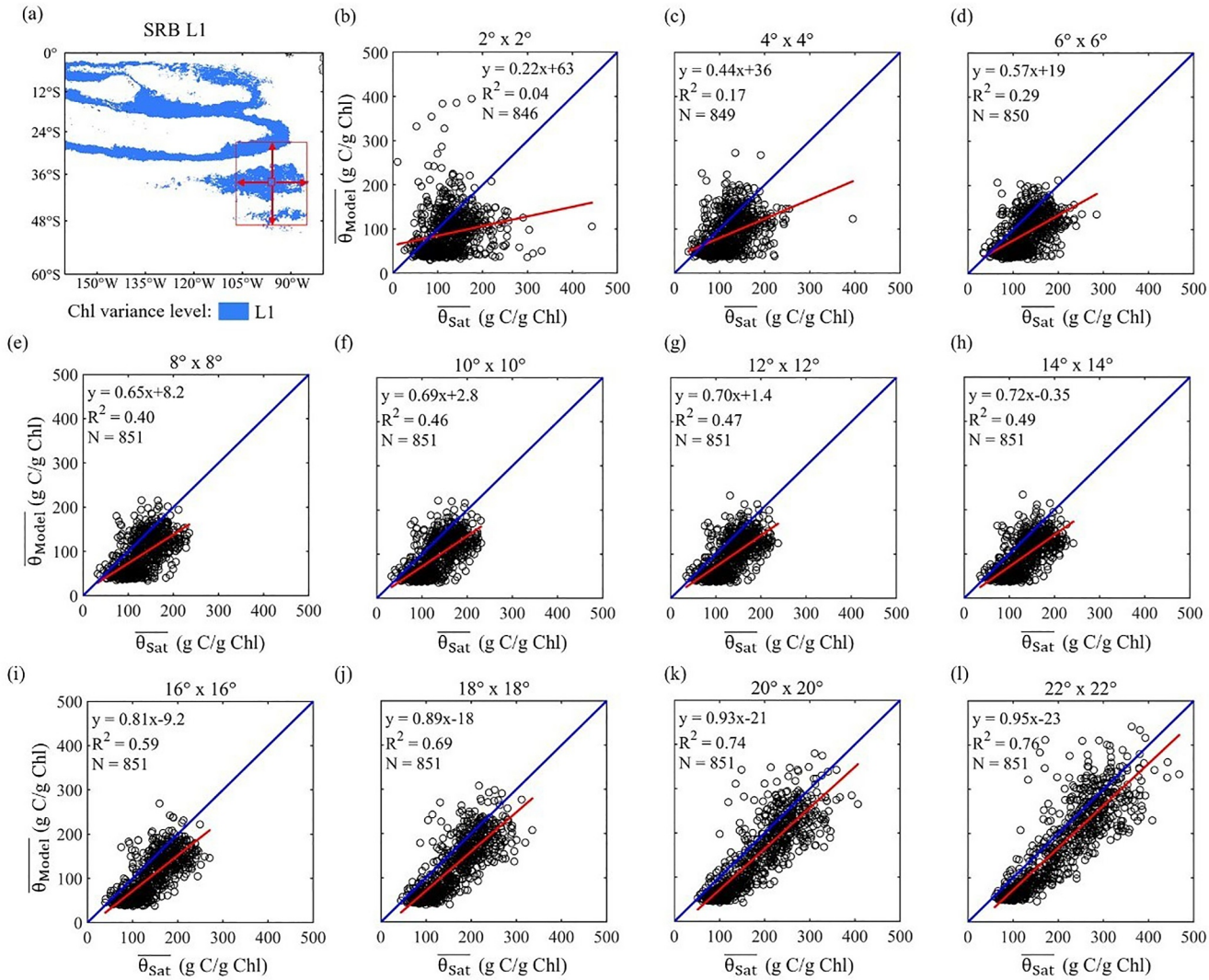

Figure 3. Relationship between $\overline{\theta_{Sat}}$ and $\overline{\theta_{Model}}$ in South Random Bin (SRB) L1 (37°–39°S and 95°–97°W to 27°–49°S and 85°–107°W). (a) The small red box represents the initial bin, and the large box represents the expanded final bin of SRB L1. The background color represents the Chl variance level is L1, which is same as Figure 2b. (b–l) The relationships between $\overline{\theta_{Sat}}$ and $\overline{\theta_{Model}}$ with the expansion of bin size in SRB L1. The blue line is a 1:1 line, and the red line is a linear fit. *N* denotes the number of data points, calculated by first determining the θ_{Sat} and θ_{Model} values for each pixel, then averaging the values for each bin. Each plot represents the 8-day average of all pixels within the study area.

bins were denoted as: South Random Bin (SRB) L0 (from 22° to 24°S and 146°–148°W to 12°–34°S and 136°–158°W), SRB L1 (37°–39°S and 95°–97°W to 27°–49°S and 85°–107°W), and SRB L2 (40°–42°S and 146°–148°W to 30°–52°S and 136°–158°W); North Random Bin (NRB) L2 (13°–15°N and 124°–126°W to 3°–25°N and 114°–136°W) and NRB L3 (39°–41°N and 167°–169°W to 29°–51°N and 157°–179°W).

For the various bins or boxes, $\overline{\theta_{Model}}$ was compared with $\overline{\theta_{Sat}}$. It is found that all of them have a statistically significant relationship ($p < 0.01$ in *t*-test). For SRB L1, as an example, $\overline{\theta_{Sat}}$ ranged from ~10.6 to 467.7 g C (g Chl)$^{-1}$, whereas $\overline{\theta_{Model}}$ ranged from ~29.3 to 441.8 g C (g Chl)$^{-1}$ (Figure 3). However, there are significant variations in the R^2 and slope values between $\overline{\theta_{Sat}}$ and $\overline{\theta_{Model}}$ in linear regression with the lowest R^2 as 0.04 and the highest as 0.76, and the slope increased from 0.22 to 0.95. Further, all results show the lowest value for a bin size of 2° × 2°, and the values of R^2 and slope increase with bin size. This pattern is also found in other areas (see Figure 4). For instance, for SRB L2, the R^2 value between $\overline{\theta_{Sat}}$ and $\overline{\theta_{Model}}$ is 0.13 for a bin size of 2° × 2°, gradually increases as the bin size expands to 0.76 for a size of 22° × 22°, so does the slope between $\overline{\theta_{Sat}}$ and $\overline{\theta_{Model}}$. Such

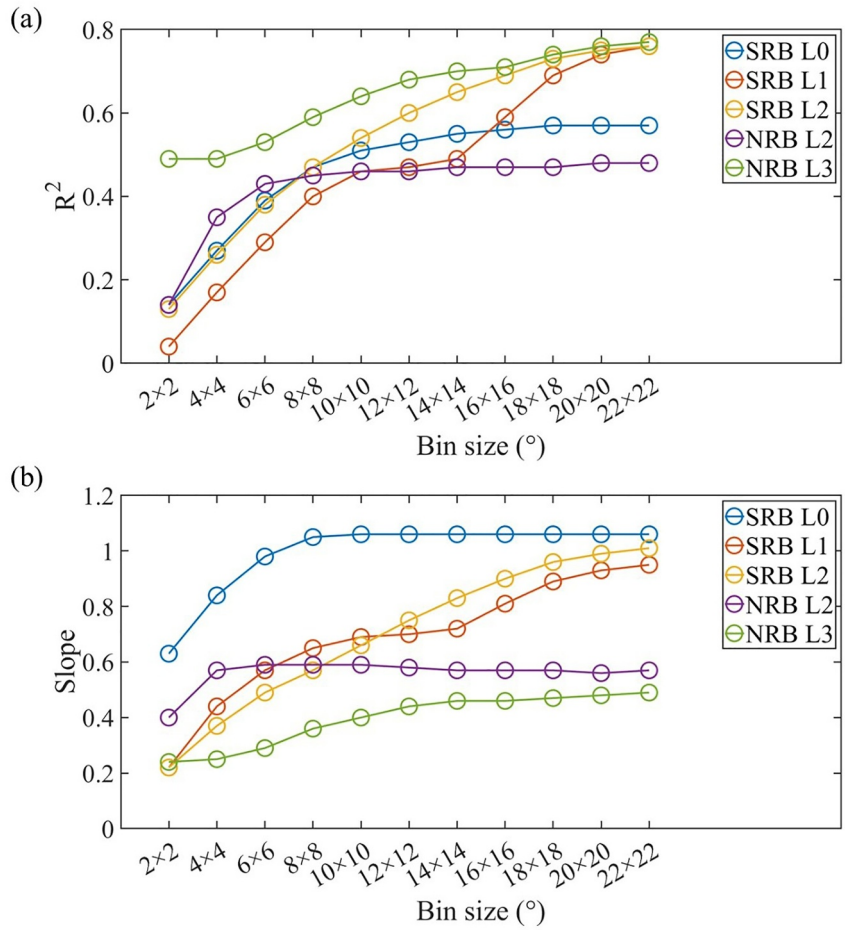

Figure 4. Relationship between $\overline{\theta_{Sat}}$ and $\overline{\theta_{Model}}$ in all five study areas (Figure 2). (a) The R^2 between $\overline{\theta_{Sat}}$ and $\overline{\theta_{Model}}$ with the bin-size expansion. The blue, orange, yellow, purple, and green lines represent South Random Bin (SRB) L0, SRB L1, SRB L2, North Random Bin (NRB) L2, and NRB L3, respectively. (b) The slopes between $\overline{\theta_{Sat}}$ and $\overline{\theta_{Model}}$ with the bin-size expansion. The color of the lines represents the same as Panel (a).

results are also observed for NRB (Figure 4) except that the rate of change in R^2 and slope values with the increase of bin size is different. For instance, for NRB L2, R^2 and slope values plateau from a bin size of 8° × 8°, but these values continue to increase for NRB L3. These results indicated that even at a single variance level of Chl, the agreement between model-estimated θ and remotely sensed θ depends on the bin size.

In general, the agreement between $\overline{\theta_{Sat}}$ and $\overline{\theta_{Model}}$ is poor when the bin size is set as 2° × 2°, but the agreement is very good when the bin size is expanded to 22° × 22°, which is consistent with the result presented by Behrenfeld et al. (2016). These results suggest that the relationship between $\overline{\theta_{Model}}$ and $\overline{\theta_{Sat}}$ is bin size dependent rather universal to any bin size.

3.2. Model Performance of Varying Bins Within the Mixed Variance Levels of Chl

Second, we focused on bin sizes across different variance levels of Chl, thereby avoiding the subjective definition of different water masses. A 5° × 5° bin was randomly selected and subsequently expanded to 35° × 35° with a 5° step (Figure 5). We then compared $\overline{\theta_{Sat}}$ with $\overline{\theta_{Model}}$ for each bin size. The randomly selected areas and bins were named as follows: SP Mbin1 (20°–25°S and 145°–150°W to 5°–40°S and 130°–165°W), SP Mbin2 (40°–45°S and 145°–150°W to 25°–60°S and 130°–165°W), and NP Mbin1 (40°–45°N and 145°–150°W to 25°–60°N and 130°–165°W).

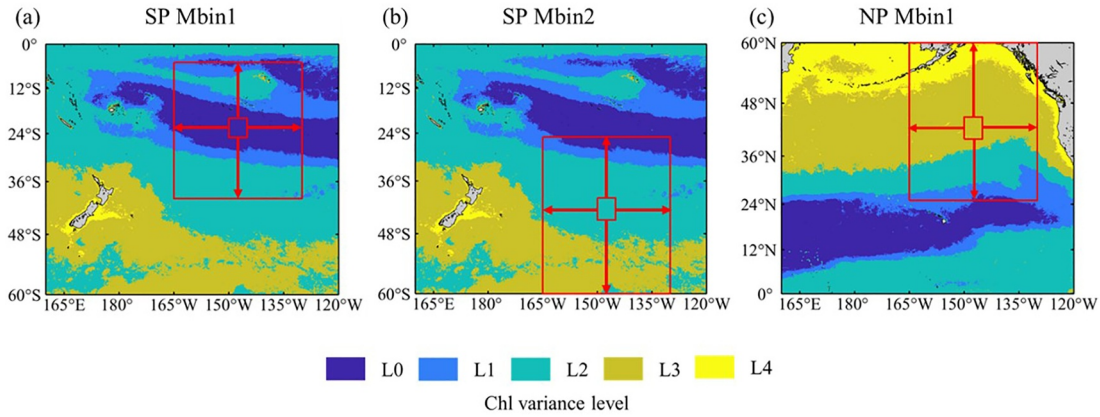

Figure 5. The study areas of bin-size expansion in mixed Chl variation levels. These random study areas are South Pacific (SP) Mbin1 (a), SP Mbin2 (b), and North Pacific Mbin1 (c), respectively. The background color of Chl variance levels is the same as Figure 2, and the light yellow is L4. The small red box represents the initial bin size (5° × 5°), and the large box represents the expanded final bin size (35° × 35°) following the directions of the arrows.

For these varying areal sizes, all of the linear regressions between $\overline{\theta_{Sat}}$ and $\overline{\theta_{Model}}$ passed the significance level ($p < 0.01$, in t-test), indicating that a statistically significant relationship exists between the two sets of values. The nature of this mixing of different Chl levels is presented in Figure 6. Specifically, for SP Mbin1, L0 is 44.8%, with L1 as 25.9%, and L2 as 29.0% (see Figure 6a). For SP Mbin2, about 68.0% is L2 with L3 as 22.6% (Figure 6b). For NP Mbin1, 25.5% belongs to L2, with 59.7% for L3, and 14.0% for other Chl variance levels especially when the bin sizes were larger than 20° × 20° (Figure 6c). All these results indicate different marine environments for these bins.

For SP Mbin2, the range of $\overline{\theta_{Sat}}$ is ~31.4–474.0 g C (g Chl)$^{-1}$, and the $\overline{\theta_{Model}}$ is ~29.7–486.2 g C (g Chl)$^{-1}$ (Figure 7). From linear regression analyses between $\overline{\theta_{Sat}}$ and $\overline{\theta_{Model}}$, the slopes increase from 0.30 to 1.05 as the

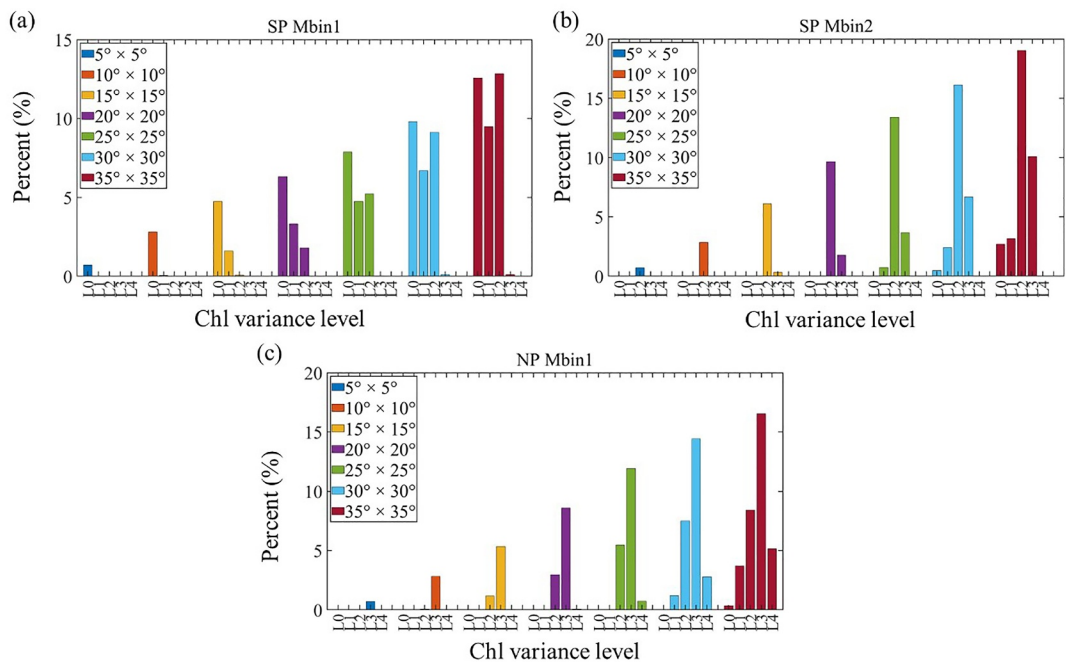

Figure 6. The relative contribution of each Chl variance level to all the pixels with valid numerical values in South Pacific (SP) Min1 (20–25°S and 145–150°W to 5–40°S and 130–165°W, a), SP Min2 (40–45°S and 145–150°W to 25–60°S and 130–165°W, b), and North Pacific Min1 (40–45°N and 145–150°W to 25–60°N and 130–165°W, c). The different colors of the bars represent different sizes of bins.

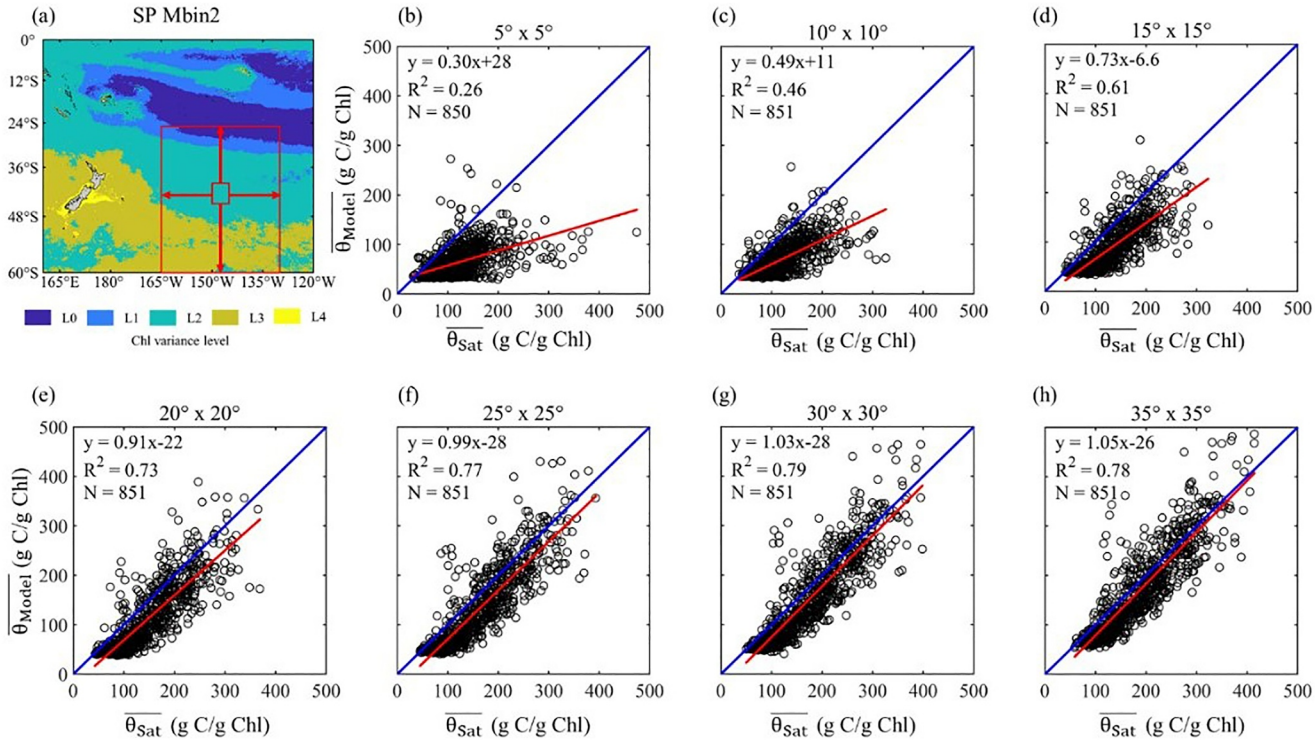

Figure 7. Relationship between $\overline{\theta_{Sat}}$ and $\overline{\theta_{Model}}$ in South Pacific (SP) Mbin2 (40–45°S and 145–150°W to 25–60°S and 130–165°W). (a) The small red box represents the initial bin, and the large box represents the expanded final bin of SP Mbin2. The background color represents the Chl variance levels, which were the same as Figure 5b. (b–h) The relationships between $\overline{\theta_{Sat}}$ and $\overline{\theta_{Model}}$ with the expansion of bin size in SP Mbin2. The blue line is a 1:1 line, and the red line is a linear fit. N denotes the number of data points, calculated by first determining the θ_{Sat} and θ_{Model} values for each pixel, then averaging the values for each bin. Each plot represents the 8-day average of all pixels within the study area.

bin size increases from 5° × 5°–35° × 35°. The R^2 value between $\overline{\theta_{Sat}}$ and $\overline{\theta_{Model}}$ is 0.26 for the 5° × 5° bin, increases gradually with the bin expansion, and eventually stabilizes at 0.78 when the bin size is 35° × 35°. Similar results are also found in the SP Mbin1 (see Figure 8). We found that the R^2 between $\overline{\theta_{Sat}}$ and $\overline{\theta_{Model}}$ increases from 0.32 to 0.75 with the bin size expanded by 5° increments. Meanwhile, the slopes between $\overline{\theta_{Sat}}$ and $\overline{\theta_{Model}}$ increase from 0.89 to 1.10 when the bin expanded from 5° × 5°–35° × 35°.

For the NP Mbin1, as the bin size expanded, we also observed an increase in the slope (from 0.28 to 0.56) between $\overline{\theta_{Sat}}$ and $\overline{\theta_{Model}}$ (see Figures 8 and 9). However, although the R^2 value between $\overline{\theta_{Sat}}$ and $\overline{\theta_{Model}}$ increases from 0.60 to 0.67 when the bin expands from 5° × 5°–10° × 10°, it decreases from 0.66 to 0.44 when the bin size further expands to 35° × 35°. These results are quite different from those observed for SP Mbin1 and SP Mbin2 where the R^2 value between $\overline{\theta_{Sat}}$ and $\overline{\theta_{Model}}$ increases gradually with bin size.

This discrepancy might be attributed to the increased inclusion of pixels from L0, L1, and L4 within the bin as it expanded from 15° × 15° to 35° × 35° for NP Mbin1 (Figure 6c). It is noticed that the agreements between $\overline{\theta_{Sat}}$ and $\overline{\theta_{Model}}$ in L0, L1, and L4 are not as good as other bins (Behrenfeld et al., 2016). This difference in performance could be the reason for the initial increase and subsequent decrease in the R^2, as more L1 and L4 pixels are encountered when the bin size is further expanded. In addition, the agreements between $\overline{\theta_{Sat}}$ and $\overline{\theta_{Model}}$ in L0, L1, and L4 in the NP are worse than those in the SP (Behrenfeld et al., 2016). Nevertheless, the slope value between $\overline{\theta_{Sat}}$ and $\overline{\theta_{Model}}$ improves as bin size increases (Figure 9), indicating an overall better alignment between $\overline{\theta_{Sat}}$ and $\overline{\theta_{Model}}$ for larger bin sizes in NP Mbin1.

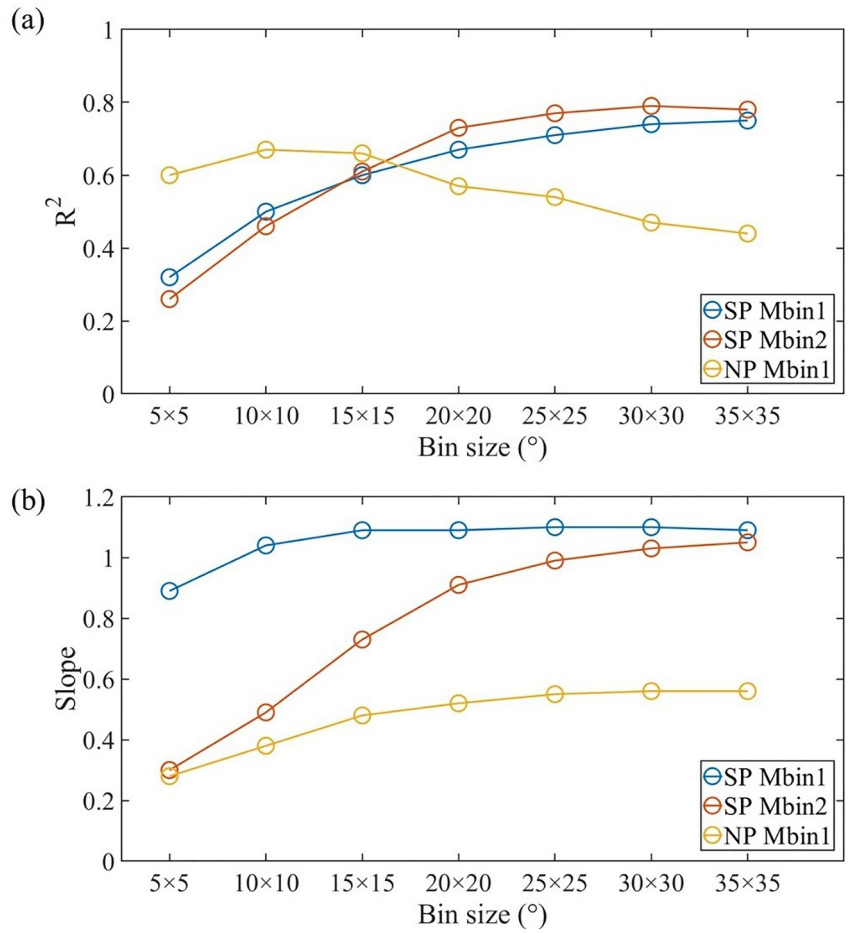

Figure 8. Relationship between $\overline{\theta_{\text{Sat}}}$ and $\overline{\theta_{\text{Model}}}$ in all three study areas (Figure 5). (a) The R^2 between $\overline{\theta_{\text{Sat}}}$ and $\overline{\theta_{Model}}$ with the bin-size expansion. The blue, orange, and yellow lines represent South Pacific (SP) Mbin1, SP Mbin2, and North Pacific Mbin1, respectively. (b) The slopes between $\overline{\theta_{\text{Sat}}}$ and $\overline{\theta_{\text{Model}}}$ with the bin-size expansion. The color of the lines represents the same as Panel (a).

4. Discussion

4.1. Model Performance at Pixel Level

Our results show that only when the bin size is similar to that presented by Behrenfeld et al. (2016), $\overline{\theta_{\text{Model}}}$ is found in good agreement with $\overline{\theta_{\text{Sat}}}$. The difference between $\overline{\theta_{\text{Model}}}$ and $\overline{\theta_{\text{Sat}}}$ becomes large when the bin size is reduced. To better understand the cause of this scale-dependent divergence, we examined the model's performance at the pixel level and compared it with its behavior at a large spatial scale.

Figure 10a is the map of SP L1, and Figure 10b shows a scatterplot between $\theta_{\text{Sat-pix}}$ and $\theta_{\text{Model-pix}}$ within SP L1 with downloaded data for a period (8-day) of 27 December to 31 December 2018, where each pixel represents a 9 km × 9 km aggregate from MODIS measurements. For this bin, where the s.d.Chl is from 0.018 to 0.026 mg m^{-3}. The ranges of $\theta_{\text{Sat-pix}}$ and $\theta_{\text{Model-pix}}$, respectively, are ~0–2,900 g C (g Chl)$^{-1}$ and ~0–3,800 g C (g Chl)$^{-1}$, whereas their averages appear quite consistent (281.2 g C (g Chl)$^{-1}$ for $\overline{\theta_{\text{Sat}}}$ and 279.6 g C (g Chl)$^{-1}$ for $\overline{\theta_{\text{Model}}}$). However, as showing in Figure 10b, there are large differences between $\theta_{\text{Sat-pix}}$ and $\theta_{\text{Model-pix}}$. Thus, not surprising to observe different performances of the photoacclimation model when different areas (or bins) were used to obtain areal averages as illustrated in Figure 10c.

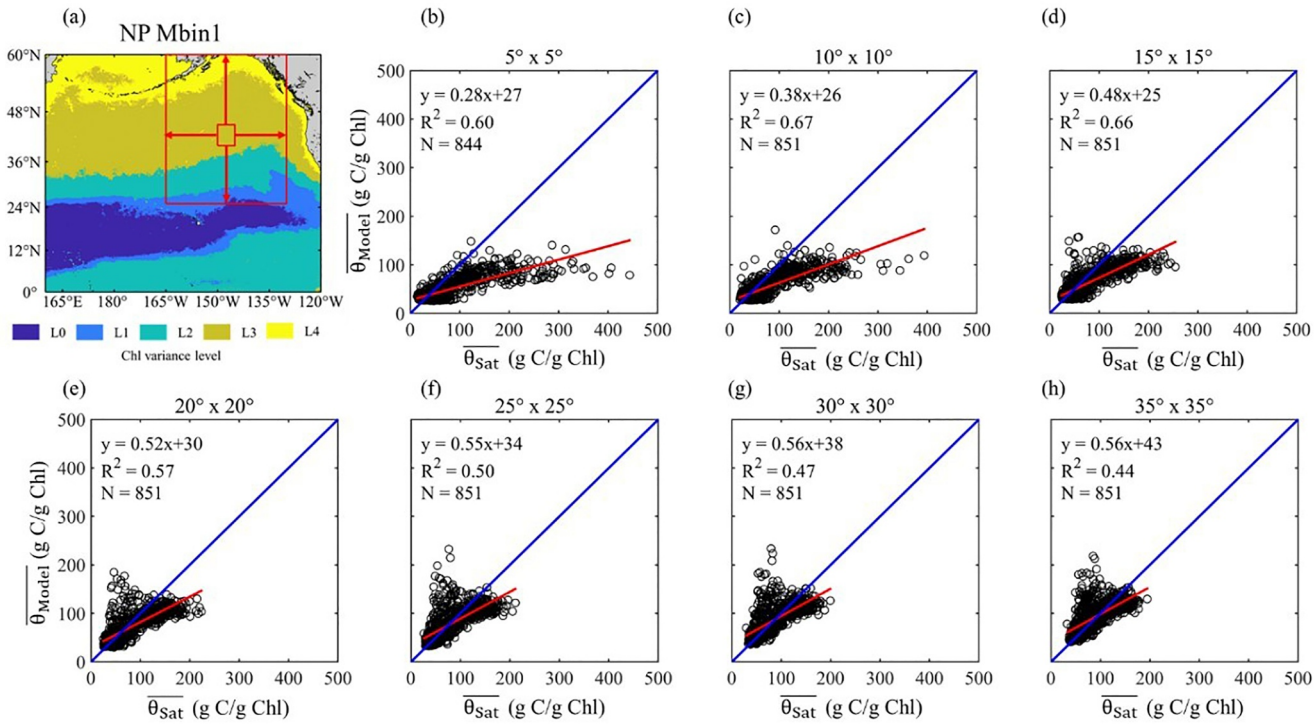

Figure 9. Relationship between $\overline{\theta_{Sat}}$ and $\overline{\theta_{Model}}$ in North Pacific (NP) Mbin1 (40°–45°N and 145°–150°W to 25°–60° N and 130°–165°W). (a) The small red box represents the initial bin, and the large box represents the expanded final bin of NP Mbin1. The background color represents the Chl variance levels, which were the same as Figure 5c. (b–h) The relationships between $\overline{\theta_{Sat}}$ and $\overline{\theta_{Model}}$ with the expansion of bin size in NP Mbin1. The blue line is a 1:1 line, and the red line is a linear fit. N denotes the number of data points, calculated by first determining the θ_{Sat} and θ_{Model} values for each pixel, then averaging the values for each bin. Each plot represents the 8-day average of all pixels within the study area.

Two bins with a size of 4° × 4° were randomly selected from SP L1 shown in Figure 10a, which were denoted as SP L1 test 1 (SPL1-t1, 15°–19°S and 118°–122°W) and SP L1 test 2 (SPL1-t2, 27°–31°S and 104°–108°W). The two boxes are shown in Figure 10c, which encompasses $\theta_{Sat\text{-}pix}$ versus $\theta_{Model\text{-}pix}$ corresponding to SPL1-t1 and SPL1-t2. For these small and subregion boxes/bins, due to significantly different behaviors between $\theta_{Sat\text{-}pix}$ and $\theta_{Model\text{-}pix}$, the $\overline{\theta_{Sat}}$ versus $\overline{\theta_{Model}}$, respectively, are quite far apart. Specifically, For SPL1-t1, the $\overline{\theta_{Sat}}$ and $\overline{\theta_{Model}}$ are 212.4 C (g Chl)$^{-1}$ and 108.4 g C (g Chl)$^{-1}$, respectively; whereas, for SPL1-t2, the $\overline{\theta_{Sat}}$ and $\overline{\theta_{Model}}$ are 801.1 g C (g Chl)$^{-1}$ and 905.8 g C (g Chl)$^{-1}$, respectively. These results demonstrate that despite apparent agreement in large-scale averages, the differences between model estimates and satellite observations at the pixel level can be substantial.

4.2. Improving the Performance of the Photoacclimation Model With Different Model Coefficients

The reduced agreement between satellite-derived and model-estimated θ at smaller spatial scales might also be influenced by other ecological and biogeochemical variability beyond photoacclimation, such as phytoplankton community composition, pigment variability, trophic interactions, and so on (Bianchi et al., 2002; Chung et al., 2012; Hung & Gong, 2011; Shih et al., 2020; Xing et al., 2014). However, these processes are also present at larger spatial scales where the model is found to perform reasonably well. This suggests that such ecological and biogeochemical processes are not the primary cause of the reduced performance. Instead, this deterioration is more likely attributable to limitations in the model's parameterization. In particular, the model coefficients (c_1 and c_2 in Equation 2) were specifically tuned based on the 37 aggregated spatial bins (i.e., L0 to L4) of the global ocean.

Figure 11 shows a case study in a randomly selected region in SP Mbin2 (35°–50°S, 140°–155°W, hereafter referred to as SP Mbin2 15° × 15°, Figure 11a). We compared the model performance using the original parameters (c_1 = 19 g C (g Chl)$^{-1}$, c_2 = 0.038 m^{-1} (Einstein m^{-2} hr^{-1})$^{-0.45}$, Figure 11b) with that obtained using

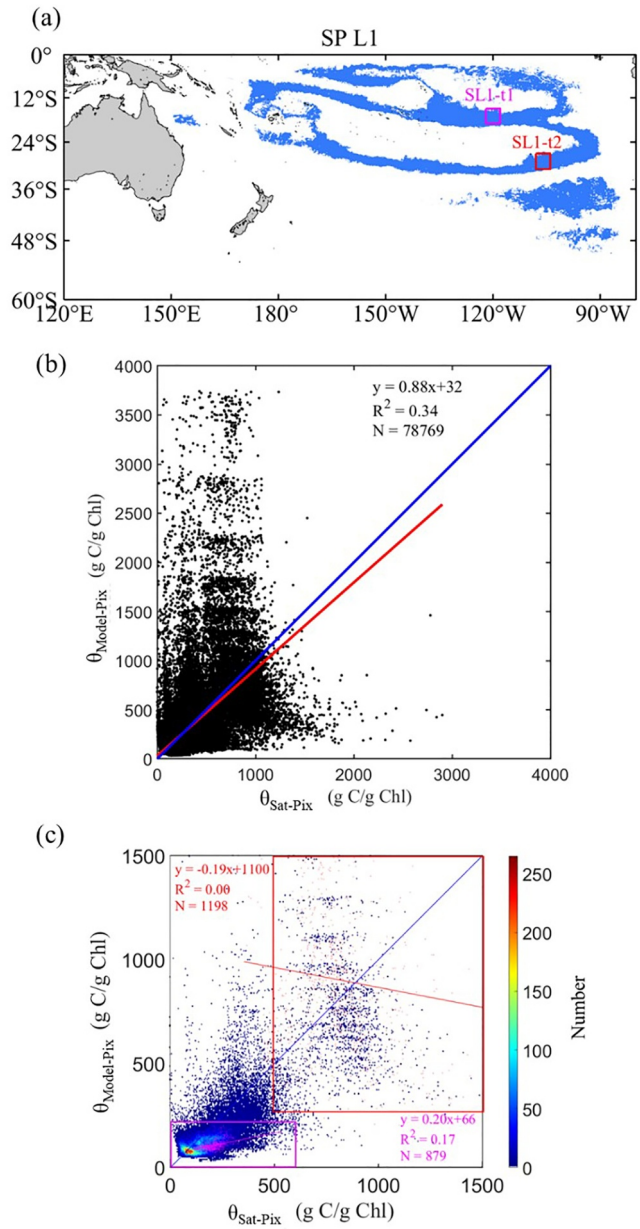

Figure 10. The relationships between $\theta_{\text{Sat-Pix}}$ and $\theta_{\text{Model-Pix}}$ in South Pacific (SP) L1 and two random bins during a randomly chosen 8-day period (December 27th to 31 December 2018). (a) Map of SP L1, with background color representing the Chl variance level (as in Figure 2). Two random selected small bins, SL1-t1 (magenta box) and SL1-t2 (red box), were randomly selected from SP L1. (b) The relationships between $\theta_{\text{Sat-pix}}$ and $\theta_{\text{Model-pix}}$ in SP L1. The blue line is a 1:1 line, and the red line is a linear fit. (c) Density plot based on data from panel (b), that is, the background color represents the density plot of SP L1 with warmer colors indicating higher pixel densities. The magenta and red boxes show the results of SL1-t1 and SL1-t2, respectively. The magenta and red boxes show the linear relationships between $\theta_{\text{Sat-pix}}$ and $\theta_{\text{Model-pix}}$ for SL1-t1 and SL1-t2, respectively, with corresponding regression lines, equations, and R^2 values in matching colors.

optimized parameters ($c_1 = 32$ g C (g Chl)$^{-1}$, $c_2 = 0.035$ m^{-1} (Einstein m^{-2} hr^{-1})$^{-0.45}$, Figure 11c). The results show a substantial improvement in fit ($R^2 = 0.62$), and the fitted regression line nearly coincides with the 1:1 line (slope ≈ 1.00), indicating a strong agreement between $\overline{\theta_{\text{Sat}}}$ and $\overline{\theta_{\text{Model}}}$ after re-tuning the model coefficients for this specific area. This example suggests that the values of c_1 and c_2 in Equation 2 are area dependent; therefore, it is necessary, although with considerable challenge, to incorporate such size information into the model.

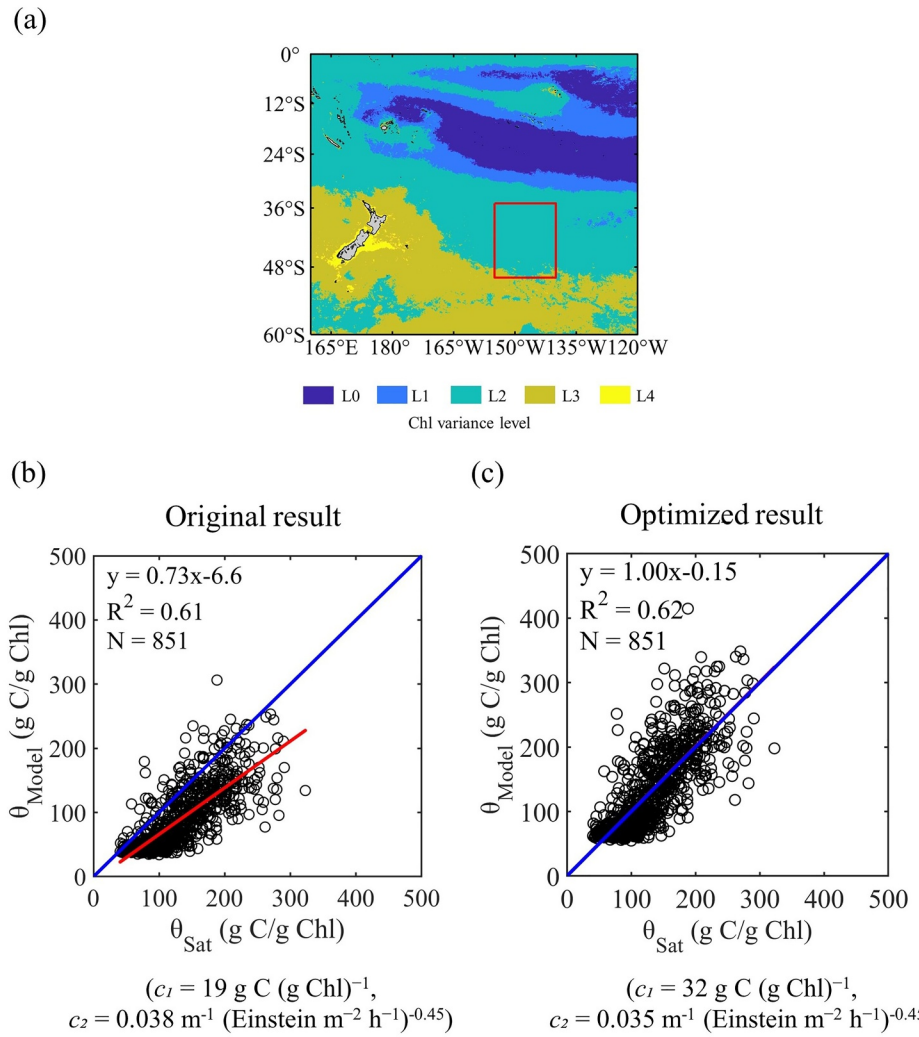

Figure 11. Relationship comparisons between $\overline{\theta_{Sat}}$ and $\overline{\theta_{Model}}$ in South Pacific (SP) Mbin2 15° × 15° region (35°–50°S, 140°–155°W). (a) The red box is the random selected study area in SP Mbin2 15° × 15° region. The background colors represent the Chl variance levels, which is same as Figure 2. (b) Relationship between $\overline{\theta_{Sat}}$ and $\overline{\theta_{Model}}$ under the original parameterization (c_1 = 19 g C (g Chl)$^{-1}$, c_2 = 0.038 m^{-1} (Einstein m^{-2} hr^{-1})$^{-0.45}$) from Behrenfeld et al. (2016). (c) Optimized result using adjusted parameters (c_1 = 32 g C (g Chl)$^{-1}$, c_2 = 0.035 m^{-1} (Einstein m^{-2} hr^{-1})$^{-0.45}$). The blue line is a 1:1 line, and the red line is a linear fit. N denotes the number of data points, calculated by first determining the $\overline{\theta_{Sat}}$ and $\overline{\theta_{Model}}$ values for each pixel, then averaging the values for each bin. Each plot represents the 8-day average of all pixels within the study area.

Additionally, temporal resolution may also impact the model's applicability. The model coefficients developed by Behrenfeld et al. (2016) were originally constructed using 8-day data of 37 bins, which might inherently smooth out short-term environmental fluctuations. Key drivers such as MLD and light availability can vary substantially on shorter timescales (Gardner et al., 1999). Therefore, it remains unknown whether substituting higher-frequency inputs (e.g., daily data) into this model would yield valid results and capture ecological responses occurring at shorter timescales. Hence, future studies should also systematically assess the model's sensitivity to temporal variability and evaluate whether recalibration is necessary to extend its application to higher temporal resolutions.

5. Conclusion

Our results showed that the agreements between $\overline{\theta_{Sat}}$ and $\overline{\theta_{Model}}$ were poor when the areal sizes are significantly smaller than that used in the model development of θ. Regardless of whether the area exhibits mixed levels or

uniform levels of Chl variation, this tendency or pattern persists. A possible explanation lies in that the model coefficients c_1 and c_2 were originally derived from 37 large bins and therefore are not directly applicable to small spatial scales.

Moreover, the complexity of water masses, as supported by previous field-based observations showing that θ can vary substantially even within relatively small spatial domains in the East China Sea (Chang et al., 2003), suggests that applying large-scale results to small-scale processes may obscure fine-scale water mass characteristics. Meanwhile, diverse ocean province strategies might lead to varying output of θ_{Model} (Chassot et al., 2011; Dowell & Platt, 2009; Longhurst, 1998; Vichi et al., 2011). The uncertainty of the relationship between remotely sensed and model-calculated θ raised from the area-size dependence might influence the evaluation of growth rates, biomass dynamics, and the impacts of other influential factors of phytoplankton, thereby affecting the accuracy of other ecological and predictive models (Boyce et al., 2017; Brunet et al., 2011; Sathyendranath et al., 2009; Signorini et al., 2015). To address these challenges and improve model performance at smaller or any spatial scales, in situ observations of θ will be indispensable. To advance our understanding of phytoplankton dynamics in the global ocean, there is a need for continued efforts to establish a photoacclimation model that is applicable without size limitations.

Conflict of Interest

The authors declare no conflicts of interest relevant to this study.

Data Availability Statement

Satellite ocean color products are available at: https://oceancolor.gsfc.nasa.gov/ (NASA Goddard Space Flight Center et al., 2018). MLD are available at: https://www.hycom.org/ (HYCOM Consortium, n.d.). All results in this study are available at: https://doi.org/10.6084/m9.figshare.28770833.

Acknowledgments
We are grateful for the financial support from the National Key Research and Development Program of China (2022YFB3901703, 2022YFC3104903), the National Natural Science Foundation of China (42430107), Fujian Satellite Data Development, Co., Ltd., and Fujian Haisi Digital Technology Co., Ltd. The authors would like to thank NASA for the distribution of MODIS ocean color products and two anonymous reviewers for constructive comments.

References

Austin, R. W., & Petzold, T. J. (1981). The determination of the diffuse attenuation coefficient of sea water using the coastal zone color scanner. In J. F. R. Gower (Ed.), *Oceanography from space* (pp. 239–256). Springer US.

Behrenfeld, M. J., Boss, E., Siegel, D. A., & Shea, D. M. (2005). Carbon-based ocean productivity and phytoplankton physiology from space. *Global Biogeochemical Cycles*, *19*(1). https://doi.org/10.1029/2004gb002299

Behrenfeld, M. J., O'Malley, R. T., Boss, E. S., Westberry, T. K., Graff, J. R., Halsey, K. H., et al. (2016). Revaluating ocean warming impacts on global phytoplankton. *Nature Climate Change*, *6*(3), 323–330. https://doi.org/10.1038/nclimate2838

Bellacicco, M., Volpe, G., Colella, S., Pitarch, J., & Santoleri, R. (2016). Influence of photoacclimation on the phytoplankton seasonal cycle in the Mediterranean Sea as seen by satellite. *Remote Sensing of Environment*, *184*, 595–604. https://doi.org/10.1016/j.rse.2016.08.004

Bianchi, T. S. (2011). The role of terrestrially derived organic carbon in the coastal ocean: A changing paradigm and the priming effect. *Proceedings of the National Academy of Sciences*, *108*(49), 19473–19481. https://doi.org/10.1073/pnas.1017982108

Bianchi, T. S., Rolff, C., Widbom, B., & Elmgren, R. (2002). Phytoplankton pigments in Baltic sea seston and sediments: Seasonal variability, fluxes, and transformations. *Estuarine, Coastal and Shelf Science*, *55*(3), 369–383. https://doi.org/10.1006/ecss.2001.0911

Boyce, D. G., Petrie, B., Frank, K. T., Worm, B., & Leggett, W. C. (2017). Environmental structuring of marine plankton phenology. *Nature Ecology & Evolution*, *1*(10), 1484–1494. https://doi.org/10.1038/s41559-017-0287-3

Brunet, C., Johnsen, G., Lavaud, J., & Roy, S. (2011). Pigments and photoacclimation processes. In S. Roy, C. A. Llewellyn, E. S. Egeland, & G. Johnsen (Eds.), *Phytoplankton pigments: Characterization, chemotaxonomy and applications in oceanography* (pp. 445–471). Cambridge University Press.

Burt, W. J., Westberry, T. K., Behrenfeld, M. J., Zeng, C., Izett, R. W., & Tortell, P. D. (2018). Carbon: Chlorophyll ratios and net primary productivity of subarctic Pacific surface waters derived from autonomous shipboard sensors. *Global Biogeochemical Cycles*, *32*(2), 267–288. https://doi.org/10.1002/2017gb005783

Chang, J., Shiah, F.-K., Gong, G.-C., & Chiang, K. P. (2003). Cross-shelf variation in carbon-to-chlorophyll a ratios in the East China Sea, summer 1998. *Deep Sea Research Part II: Topical Studies in Oceanography*, *50*(6–7), 1237–1247. https://doi.org/10.1016/s0967-0645(03)00020-1

Chassot, E., Bonhommeau, S., Reygondeau, G., Nieto, K., Polovina, J., Huret, M., et al. (2011). Satellite remote sensing for an ecosystem approach to fisheries management. *ICES Journal of Marine Science*, *68*(4), 651–666. https://doi.org/10.1093/icesjms/fsq195

Chung, C.-C., Gong, G.-C., & Hung, C.-C. (2012). Effect of typhoon Morakot on microphytoplankton population dynamics in the subtropical northwest Pacific. *Marine Ecology Progress Series*, *448*, 39–49. https://doi.org/10.3354/meps09490

da Silveira Bueno, C., Paytan, A., de Souza, C. D., & Franco, T. T. (2024). Global warming and coastal protected areas: A study on phytoplankton abundance and sea surface temperature in different regions of the Brazilian south Atlantic coastal ocean. *Ecology and Evolution*, *14*(8), e11724. https://doi.org/10.1002/ece3.11724

Dowell, M., & Platt, T. (2009). Partition of the ocean into ecological provinces: Role of ocean-colour radiometry.

Dutkiewicz, S., Hickman, A. E., Jahn, O., Henson, S., Beaulieu, C., & Monier, E. (2019). Ocean colour signature of climate change. *Nature Communications*, *10*(1), 578. https://doi.org/10.1038/s41467-019-08457-x

Fox, J., Behrenfeld, M. J., Haëntjens, N., Chase, A., Kramer, S. J., Boss, E., et al. (2020). Phytoplankton growth and productivity in the Western north Atlantic: Observations of regional variability from the NAAMES field campaigns. *Frontiers in Marine Science*, *7*, 24. https://doi.org/10.3389/fmars.2020.00024

Gardner, W. D., Gundersen, J. S., Richardson, M. J., & Walsh, I. D. (1999). The role of seasonal and diel changes in mixed-layer depth on carbon and chlorophyll distributions in the Arabian Sea. *Deep Sea Research Part II: Topical Studies in Oceanography*, *46*(8–9), 1833–1858. https://doi.org/10.1016/s0967-0645(99)00046-6

Gerald, B. (2018). A brief review of independent, dependent and one sample t-test. *International Journal of Applied Mathematics and Theoretical Physics*, *4*(2), 50. https://doi.org/10.11648/j.ijamtp.20180402.13

He, Q., Zhan, H., Cai, S., & Zhan, W. (2021). Eddy-induced near-surface chlorophyll anomalies in the subtropical gyres: Biomass or physiology? *Geophysical Research Letters*, *48*(7), e2020GL091975. https://doi.org/10.1029/2020gl091975

Hu, C., Lee, Z., & Franz, B. (2012). Chlorophyll algorithms for oligotrophic oceans: A novel approach based on three-band reflectance difference. *Journal of Geophysical Research*, *117*(C1). https://doi.org/10.1029/2011jc007395

Hung, C.-C., & Gong, G.-C. (2011). Biogeochemical responses in the southern East China Sea after typhoons. *Oceanography*, *24*(4), 42–51. https://doi.org/10.5670/oceanog.2011.93

Hung, C. C., Gong, G. C., Chou, W. C., Chung, C. C., Lee, M. A., Chang, Y., et al. (2010). The effect of typhoon on particulate organic carbon flux in the southern East China Sea. *Biogeosciences*, *7*(10), 3007–3018. https://doi.org/10.5194/bg-7-3007-2010

HYCOM Consortium. (n.d.). HYCOM GLBa0.08, experiment 90.8 [Dataset]. *Global 1/12° Analysis (archival product)*. Retrieved from https://www.hycom.org/data/glba0pt08

Kirk, J. (1983). *Light and photosynthesis in aquatic ecosystems*. Cambridge University Press.

Letelier, R. M., Bidigare, R. R., Hebel, D. V., Ondrusek, M., Winn, C., & Karl, D. M. (1993). Temporal variability of phytoplankton community structure based on pigment analysis. *Limnology & Oceanography*, *38*(7), 1420–1437. https://doi.org/10.4319/lo.1993.38.7.1420

Liu, Q., Pan, D., Bai, Y., Wu, K., Chen, C.-T. A., Sun, J., & Zhang, L. (2013). The satellite reversion of dissolved organic carbon (DOC) based on the analysis of the mixing behavior of DOC and colored dissolved organic matter: The East China Sea as an example. *Acta Oceanologica Sinica*, *32*(2), 1–11. https://doi.org/10.1007/s13131-013-0272-x

Longhurst, A. R. (1998). *Ecological geography of the sea*. Academic Press.

Maritorena, S., Siegel, D. A., & Peterson, A. R. (2002). Optimization of a semianalytical ocean color model for global-scale applications. *Applied Optics*, *41*(15), 2705–2714. https://doi.org/10.1364/ao.41.002705

Mignot, A., Claustre, H., Uitz, J., Poteau, A., d'Ortenzio, F., & Xing, X. (2014). Understanding the seasonal dynamics of phytoplankton biomass and the deep chlorophyll maximum in oligotrophic environments: A bio-argo float investigation. *Global Biogeochemical Cycles*, *28*(8), 856–876. https://doi.org/10.1002/2013gb004781

Morel, A., Huot, Y., Gentili, B., Werdell, P. J., Hooker, S. B., & Franz, B. A. (2007). Examining the consistency of products derived from various ocean color sensors in open ocean (case 1) waters in the perspective of a multi-sensor approach. *Remote Sensing of Environment*, *111*(1), 69–88. https://doi.org/10.1016/j.rse.2007.03.012

Mueller, J. L. (2000). SeaWiFS algorithm for the diffuse attenuation coefficient, K (490), using water-leaving radiances at 490 and 555 nm. *SeaWiFS postlaunch calibration and validation analyses, part*, *3*, 24–27.

NASA Goddard Space Flight Center, Ocean Ecology Laboratory, Ocean Biology Processing Group. (2018). Moderate resolution imaging spectroradiometer (MODIS) aqua chlorophyll concentration (9 km, 8-day, version 2018.0) [Dataset]. *NASA/OB.DAAC*. https://doi.org/10.5067/AQUA/MODIS/L3M/CHL/2018

Sathyendranath, S., Stuart, V., Nair, A., Oka, K., Nakane, T., Bouman, H., et al. (2009). Carbon-to-chlorophyll ratio and growth rate of phytoplankton in the sea. *Marine Ecology Progress Series*, *383*, 73–84. https://doi.org/10.3354/meps07998

Sharma, P., Marinov, I., Cabre, A., Kostadinov, T., & Singh, A. (2019). Increasing biomass in the warm oceans: Unexpected new insights from SeaWiFS. *Geophysical Research Letters*, *46*(7), 3900–3910. https://doi.org/10.1029/2018gl079684

Shih, Y.-Y., Hung, C.-C., Huang, S.-Y., Muller, F. L. L., & Chen, Y.-H. (2020). Biogeochemical variability of the upper ocean response to typhoons and storms in the northern South China Sea. *Frontiers in Marine Science*, 7.

Signorini, S. R., Franz, B. A., & McClain, C. R. (2015). Chlorophyll variability in the oligotrophic gyres: Mechanisms, seasonality and trends. *Frontiers in Marine Science*, *2*. https://doi.org/10.3389/fmars.2015.00001

Swan, C. M., Siegel, D. A., Nelson, N. B., Carlson, C. A., & Nasir, E. (2009). Biogeochemical and hydrographic controls on chromophoric dissolved organic matter distribution in the Pacific Ocean. *Deep Sea Research Part I: Oceanographic Research Papers*, *56*(12), 2175–2192. https://doi.org/10.1016/j.dsr.2009.09.002

Tang, S., Chen, C., Zhan, H., Zhang, J., & Yang, J. (2008). An appraisal of surface chlorophyll estimation by satellite remote sensing in the South China Sea. *International Journal of Remote Sensing*, *29*(21), 6217–6226. https://doi.org/10.1080/01431160802175579

Vichi, M., Allen, J. I., Masina, S., & Hardman-Mountford, N. J. (2011). The emergence of ocean biogeochemical provinces: A quantitative assessment and a diagnostic for model evaluation. *Global Biogeochemical Cycles*, *25*(2). https://doi.org/10.1029/2010gb003867

Werdell, P. J., & Bailey, S. W. (2005). An improved in-situ bio-optical data set for ocean color algorithm development and satellite data product validation. *Remote Sensing of Environment*, *98*(1), 122–140. https://doi.org/10.1016/j.rse.2005.07.001

Westberry, T., Behrenfeld, M. J., Siegel, D. A., & Boss, E. (2008). Carbon-based primary productivity modeling with vertically resolved photoacclimation. *Global Biogeochemical Cycles*, *22*(2). https://doi.org/10.1029/2007gb003078

Xing, X., Claustre, H., Uitz, J., Mignot, A., Poteau, A., & Wang, H. (2014). Seasonal variations of bio-optical properties and their interrelationships observed by bio-argo floats in the subpolar north Atlantic. *Journal of Geophysical Research: Oceans*, *119*(10), 7372–7388. https://doi.org/10.1002/2014jc010189

Xing, X., Qiu, G., Boss, E., & Wang, H. (2019). Temporal and vertical variations of particulate and dissolved optical properties in the South China Sea. *Journal of Geophysical Research: Oceans*, *124*(6), 3779–3795. https://doi.org/10.1029/2018jc014880

Xiu, P., & Chai, F. (2021). Impact of atmospheric deposition on carbon export to the deep ocean in the subtropical northwest Pacific. *Geophysical Research Letters*, *48*(6), e2020GL089640. https://doi.org/10.1029/2020gl089640

Yamaguchi, R., Rodgers, K. B., Timmermann, A., Stein, K., Schlunegger, S., Bianchi, D., et al. (2022). Trophic level decoupling drives future changes in phytoplankton bloom phenology. *Nature Climate Change*, *12*(5), 469–476. https://doi.org/10.1038/s41558-022-01353-1

Yang, B., Fox, J., Behrenfeld, M. J., Boss, E. S., Haëntjens, N., Halsey, K. H., et al. (2021). In situ estimates of net primary production in the Western north Atlantic with argo profiling floats. *Journal of Geophysical Research: Biogeosciences*, *126*(2), e2020JG006116. https://doi.org/10.1029/2020jg006116